

# Rational Design of Peptide Biorecognition Elements on Carbon Nanotubes for Sensing Volatile Organic Compounds

Daniel Sim, Zhifeng Kuang, Gustavo Sant'Anna, Rachel M. Krabacher, Michael C. Brothers, Jorge L. Chávez, Jennifer A. Martin, Ahmad E. Islam, Benji Maruyama, Rajesh R. Naik, Nicholas M. Bedford, and Steve S. Kim\*

Carbon nanotube (CNT) chemiresistors have emerged as miniaturized platforms for wearable volatile organic compound (VOC) sensors. As a promising biorecognition element (BRE), a short peptide can functionalize CNT to be sensitive and selective to target VOCs. However, unveiling the VOC-optimized peptide-CNT pair for gas-phase sensing remains unclear. Here, a novel multimodal molecular toolset for designing, building, and probing suitable BRE-CNT sensors using machine learning, molecular dynamics, and near-edge X-ray absorption fine structure spectroscopy is presented. This computational and experimental suite predicts the peptide conformation on the CNT surface and probes how the peptide-CNT interfaces affect the VOC sensing. Then, peptide-functionalized CNT chemiresistors are tested against various VOCs to confirm the efficacy of the toolkit. The results show that the vertically oriented peptide on the CNT surface hinders VOC access to the peptide-CNT interface, resulting in a significantly lower sensor signal than the CNT chemiresistor with the horizontally oriented peptide. The interactive computational and experimental results strongly indicate that a peptide conformation plays an important role in VOC sensing sensitivity.

compounds. Exhaled breath is one of the most accessible and zero-invasive samples to monitor human health and performance. For example, recent studies have demonstrated that analyzing the exhaled breath is practical for fast-diagnosing of COVID-19.<sup>[1,2]</sup> Volatile organic compounds (VOCs)<sup>[3–6]</sup> in the exhaled breath serve as performance-related biomarkers providing rich information on human physiological/physical statuses<sup>[7–11]</sup> such as psychological stress and fatigue level. A miniaturized sensor is key to building a wearable sensing suite with the capability to monitor human breath. Conventional VOC detection tools are either bulky or non-selective. For example, gas chromatography–mass spectrometry (GC–MS) is accepted as a gold standard for measuring breath VOCs.<sup>[12–14]</sup> However, GC–MS is bulky due to its heating and vacuum systems and requires a long operation time due to the VOC sampling

and separation process. Photo-ionized detectors (PIDs) are another commercial off-the-shelf, portable VOC sensors commonly applied to gas sensing.<sup>[15,16]</sup> These sensors (VOC-TRAQ, MOCON, Inc., Minneapolis, MN, USA) range their dimensions

## 1. Introduction

Minimally or non-invasive human health and performance monitoring can benefit from achieving sensing for molecular

D. Sim, M. C. Brothers, J. L. Chávez, R. R. Naik, S. S. Kim  
Air Force Research Laboratory  
711th Human Performance Wing  
Wright-Patterson Air Force Base, OH 45433, USA  
E-mail: steve.kim.13@us.af.mil

D. Sim  
Research Associateship Program  
The National Academies of Sciences  
Engineering and Medicine  
Washington, DC 20001, USA

 The ORCID identification number(s) for the author(s) of this article can be found under <https://doi.org/10.1002/admi.202201707>.

© 2022 The Authors. Advanced Materials Interfaces published by Wiley-VCH GmbH. This is an open access article under the terms of the Creative Commons Attribution License, which permits use, distribution and reproduction in any medium, provided the original work is properly cited.

DOI: 10.1002/admi.202201707

D. Sim, Z. Kuang, M. C. Brothers  
Integrative Health & Performance Sciences Division  
UES, Inc  
Dayton, OH 45432, USA

Z. Kuang, R. M. Krabacher, J. A. Martin, B. Maruyama  
Air Force Research Laboratory  
Materials and Manufacturing Directorate  
Wright-Patterson Air Force Base, OH 45433, USA

G. Sant'Anna, N. M. Bedford  
School of Chemical Engineering  
The University of New South Wales  
Kensington, NSW 2052, Australia

A. E. Islam  
Air Force Research Laboratory  
Sensors Directorate  
Wright-Patterson Air Force Base, OH 45433, USA

close to 2.5 cm—diameter × 9.1 cm—length and detect an electrical current created by the ionized molecules from UV-irradiation to the VOC. However, PIDs suffer from selectivity issues<sup>[3,17]</sup> in differentiating VOCs, showing significant non-specific responses with a range of VOCs.

Meanwhile, carbon nanotube (CNT) chemiresistors<sup>[18,19]</sup> are considered the suitable sensor platforms for VOC monitoring due to their nano-sized<sup>[20]</sup> and fast electronic response enabling real-time continuous measurement.<sup>[21,22]</sup> In addition, biorecognition elements (BREs) can functionalize CNTs to provide selective and sensitive characteristics to the chemiresistors.<sup>[23–26]</sup> BREs are biological materials (i.e., enzyme, antibody, aptamer, and peptide) specific to target molecules.<sup>[27–30]</sup> Among BREs, peptides have been claimed as one of the most well-known molecular tools due to their chemical stability,<sup>[31,32]</sup> diversity,<sup>[33]</sup> and customizability.<sup>[34,35]</sup> For these reasons, many works have utilized peptides as promising sensing elements for gas detection applications.<sup>[36–41]</sup> Previously, several peptide-coated CNT chemiresistors have been developed to detect molecules of interest selectively. For example, Kim et al. and Naik et al. demonstrated selective detection of low volatile 2,4,6-Trinitrotoluene explosive by using the specific binding peptides.<sup>[21,24]</sup> Son et al. demonstrated selective detection of 3-Methyl-1-butanol (related to salmonella contamination in food) using *Drosophila* odorant-binding protein-derived peptide<sup>[42]</sup> with a 1 fM sensitivity. Although several peptide sequences have been utilized as biorecognition elements for biomarkers of interest, predicting the suitable peptide–CNT pair for volatile sensing remains unclear. To date, most BRE analyses have been done in the liquid phase using phage display and enzyme-linked immunosorbent assay (ELISA). Therefore, tools to characterize the peptide–CNT pair in the non-aqueous ambience are in high demand to advance VOC sensor development efforts.

Here, we present a novel method using the combination of machine learning, *in silico* analysis, and *in situ* near-edge X-ray absorption fine structure (NEXAFS) spectroscopy to predict the non-aqueous peptide–CNT pairs responsive to VOCs, followed by CNT chemiresistor test for *in operando* evaluation. We select isopropyl alcohol (IPA) as a target VOC since it acts as a cognitive biomarker related to central nervous system depressant.<sup>[3]</sup> First, we perform a novel machine learning using artificial neural network models to identify five IPA-responsive 7-mer peptides. Then, we utilize molecular dynamics (MD) to estimate the conformation of these peptides on the CNT surface by calculating peptide–CNT interaction energies. In addition, NEXAFS spectroscopy analyzes the alignment of the amide backbone using N K-edge measurements to further assess peptides' conformation. Finally, peptide-functionalized CNT chemiresistors are fabricated and tested against IPA to probe correlations between VOC sensing and the peptide–CNT pair characteristics. The chemiresistor results suggest that the accessible surface area determined by the peptide conformation on the CNT surface is a significant factor in VOC sensing. Our results strongly indicate that the present study can predict and optimize the peptide-based recognition element for designing the gas-phase CNT sensor with higher sensitivity.

## 2. Results and Discussion

To identify IPA-responsive 7-mer peptide sequences, we used NNAlign as an artificial neural network-based alignment method for receptor–ligand binding prediction.<sup>[43,44]</sup> This method efficiently finds underlying sequence patterns by simultaneously aligning peptide sequences and identifying motifs associated with quantitative binding affinity. It has been successfully applied in predicting peptide binding to the major histocompatibility complex (MHC) molecule. An online implementation of the method is available at <http://www.cbs.dtu.dk/services/NNAlign/>. The input to the program is a set of peptide sequences with binding affinity to a target molecule. When the peptide is uploaded to the network, the server returns a sequence alignment, a binding motif of the interaction, and a model that can be used to scan for motif occurrences in new sequences.

**Figure 1** shows the identification of the top five 7-mer peptide sequences using an artificial neural network. The detailed method is described in the Experimental Section. Briefly, we randomly generated a set of 5000 peptide sequences of 7 amino acids and inputted the binding affinity scores (i.e., interaction energies to IPA) calculated by MD simulations (Figure 1a). After uploading the sequences and interaction energies to the NNAlign web server, we used the feed-forward artificial network model with ten hidden neurons. The gradient descent back-propagation algorithm lowered the sum of the squared errors between the predicted and given binding scores. Figure 1b shows the distribution of the binding affinity scores after 500 training cycles. The tyrosine residue was found to show the highest binding weight, as shown in Figure 1c. Even if tyrosine residue showed the highest score, it seems that 7-mer peptides show an IPA affinity differently depending on the sequence combination. Consequently, we identified the top five peptide sequences (QGWYYT, FYYLLQ, MKPHYYN, TLYCFRT, and YVPRMHS) and labeled EP1, EP2, EP3, EP4, and EP5, respectively, as shown in Figure 1d.

To predict the conformation of a peptide on the CNT surface, we used the interaction energy between CNT and peptide calculated by MD simulations. Based on the experimental solution prepared with 1.5 mg peptide, 1.5 mg CNT powder, and 1.5 mL distilled water, a simulation system has at most one peptide and one CNT with chirality (10, 3) inside a cylinder with a radius of 7 nm and height of 5.2 nm. Assuming there may be many different conformations of peptides binding on the CNT surface, we performed two starting configurations where the peptide is either parallel or vertical to the CNT axis solvated in a cylinder of water, as shown in **Figure 2a**. After building the single-walled CNT and linear peptide models using Materials Studio 8.0 (©2014 Dassault Systèmes) and VMD1.9.3,<sup>[45]</sup> NAMD2.13 software package performed MD simulations to calculate the CNT interaction energies to each residue of the peptides. Detailed simulation conditions to obtain the peptide–CNT interaction energies are described in the Experimental Section. After 100 ns equilibration of peptide–CNT in water, water molecules were removed from each simulation system to mimic gas-phase conditions. After removing water, VOCs were placed 2 nm above the CNT surface. We carried

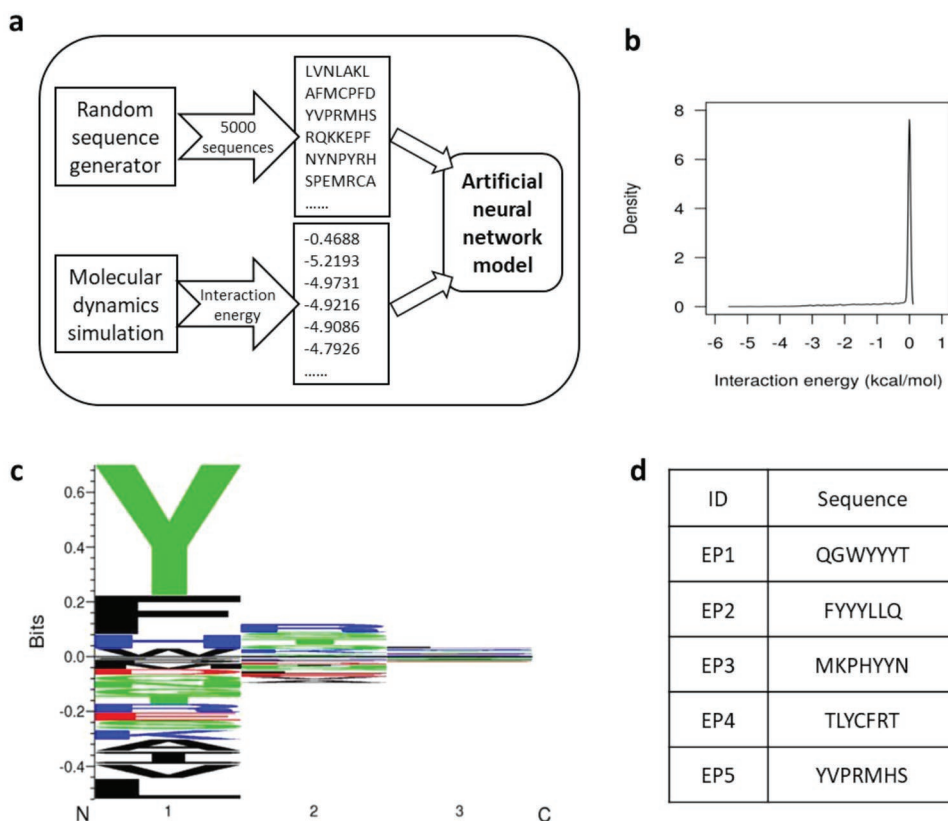


**Figure 1.** Machine learning using artificial neural networks to identify isopropyl alcohol (IPA)-responsive 7-mer peptides: a) the block diagram of the artificial neural network model; b) the raw data distribution of the binding scores (i.e., interaction energies) between peptides and IPA; c) the sequence motif showing the binding residue tyrosine recognized from the neural network modeling; d) the identified top five 7-mer peptide sequences responsive to IPA.

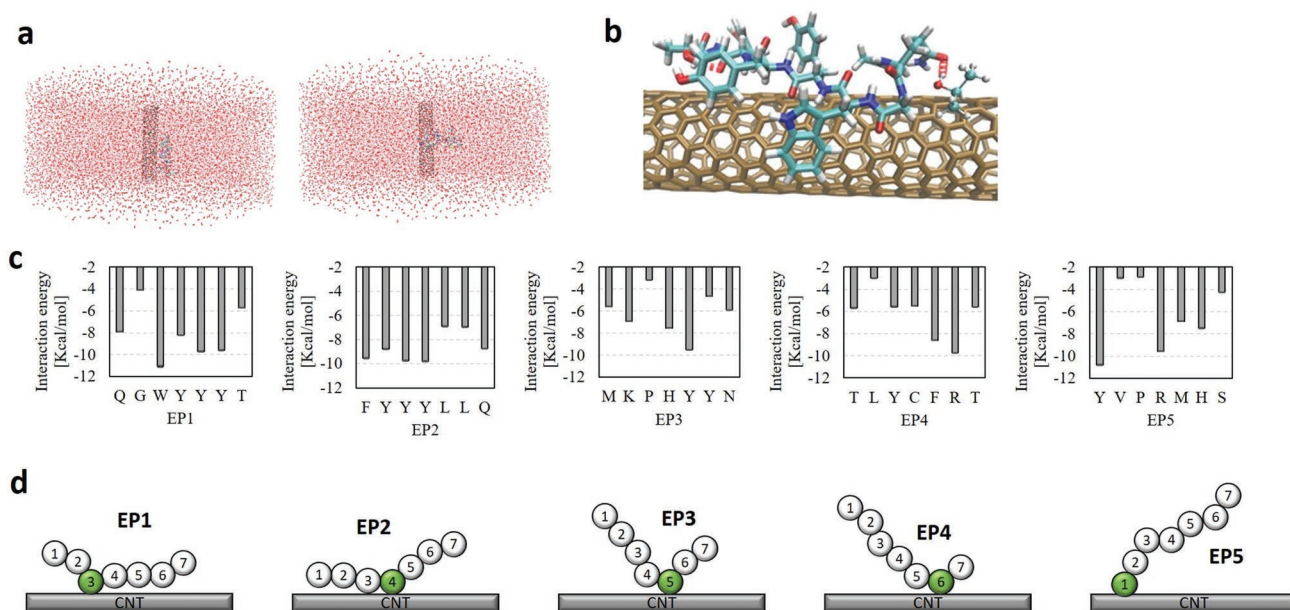


**Figure 2.** Molecular dynamic simulations to calculate interaction energies between peptide and carbon nanotube (CNT) and predict peptide conformation on CNT surface: a) the initial simulation configurations where a peptide is either parallel or vertical to CNT axis; b) the representative graphical image showing EP1 conformation on the CNT surface; c) the calculated peptides' interaction energies to CNT; d) the predicted 2-dimensional peptide conformation based on the interaction energies.

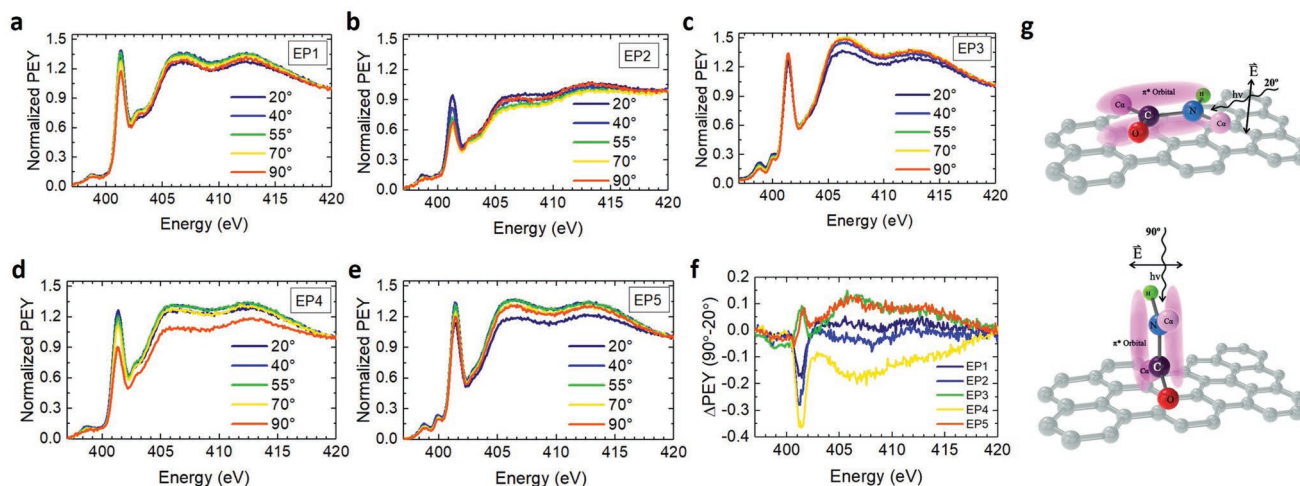


**Figure 3.** Near-edge X-ray absorption fine structure (NEXAFS) spectra to assess peptide molecular alignments: a–e) N K-edge NEXAFS spectra obtained from five different probe angles from 20° to 90° for the peptides (EP1–5) on the carbon substrate; f) differential spectra between the normal (90°) and grazing (20°) radiation incidence; g) schematics showing the difference in maximum radiation absorption depending on the peptide orientation.

out three independent 100 ns equilibrations for each system composed of CNT, a peptide, and a VOC for statistical analysis. The last 10 ns snapshots from each equilibration were used to calculate the relevant pair interaction energies. We performed the first MD simulation with water to calculate CNT interaction energy as we assembled the CNT onto chemiresistors in the aqueous phase (using a CNT–peptide solution dispersed in water and DEP process) for the chemiresistor experiment. Then the second simulation calculates VOC interaction energy without water in the simulation system to mimic gas-phase VOC exposure on the CNT chemiresistor in the gas chamber. Figure 2b shows the representative graphical image predicted by the interaction energies, describing how EP1 binds to the CNT surface. Figure 2c shows the calculated CNT interaction energies of each residue of EP1–5, respectively. Based on the calculation data, we simplified the conformation model by considering the 2D schematics of the peptide residues on the CNT surface. Because the interaction energy indicates which residue is likely to bind to CNTs, and a lower negative value of the energy explains a higher possibility of binding to CNTs, we assume that the residue having the lowest energy in a peptide serves as a *CNT-binding residue* (*CNT linker*). Then the other residues form amino acid chains differently depending on the energy level of each residue, as shown in Table S1 (Supporting Information). Using this simplified conformation model, Figure 2d shows the predicted 2D schematics of the conformations of EP1–5 to briefly describe how vertically or horizontally the peptides are oriented on the CNT surface. The residue with a green color indicates CNT linkers with strong CNT interaction energies. Based on this prediction, we found that EP1 and EP2 are horizontally oriented on the CNT, while EP3, EP4, and EP5 are more vertically oriented.

To further assess the conformation of the peptides, we utilized NEXAFS spectroscopy to analyze the peptide’s molecular alignment, whose characteristics are closely related to the peptide conformation. NEXAFS is photoelectron spectroscopy performed at low energies that relies on the transition of an

atomic core electron to an empty molecular orbital through X-ray absorption, resulting in a unique absorption fine structure. This technique is sensitive to molecular alignment since absorption events correspond to the electric field vector of the incoming X-rays being adsorbed by different orbital hybridization(s) within the molecule, which themselves are highly oriented in the covalent bonding in lighter elements.<sup>[46]</sup> NEXAFS can therefore be implemented to study molecular alignment/morphology at biosensor interfaces.<sup>[47–49]</sup> Further, it is important to note that the limited number of amino acids inherently mitigates possible secondary structure effects to the peptide orientation probed via NEXAFS, providing more succinct information about binding at the biotic/abiotic interface. Here, we used the N K-edge of EP1–EP5 samples deposited on CVD graphene to probe the amide  $\pi$  orbital functionality along the peptide backbone, aiming to obtain an overall molecular orientation on the surface.<sup>[50–52]</sup> It is worth mentioning that the amino acid residues from peptides interact non-covalently with CNT and graphene in the same qualitative way, mainly through  $\pi$ – $\pi$  stacking interactions.<sup>[53]</sup> The difference emerges in this interaction’s magnitude, reportedly weaker for CNT than graphene.<sup>[53–56]</sup> Therefore, we assumed that the peptides’ orientations are equivalent on both substrates, differing in the interaction energy values but keeping the same pattern.

Figure 3a–e shows N K-edge NEXAFS spectra obtained under five different X-ray incidence angles (20°, 40°, 55°, 70°, and 90°) for EP1–EP5 peptide sequences. The sharp peaks around 401.3 eV are associated with the N1s  $\rightarrow \pi^*$  transition of the peptide bond amide orbital. Two broader resonances dominating the spectra at higher energies around 406 and 413 eV are associated with electrons from N1s  $\rightarrow \sigma^*$  transitions of N–C and N–H bonds, respectively.<sup>[57]</sup> Features at lower energies (below 401.3 eV peak) are related to nitrogen atoms present on amino acid residues, with EP3 (Figure 3c) and EP5 (Figure 3e) showing two small shoulders from two N1s  $\rightarrow \pi^*$  of both histidine nitrogen atoms.<sup>[58,59]</sup> EP1 (Figure 3a), EP2 (Figure 3b), and EP4 (Figure 3d) showed only one small shoulder related to free

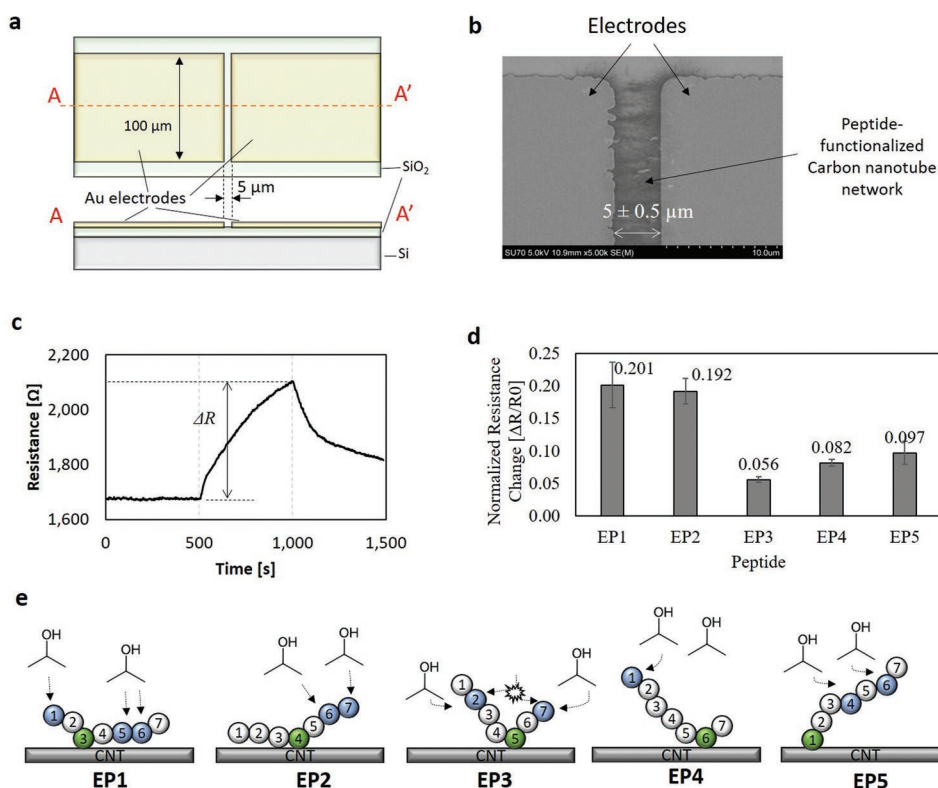


**Figure 4.** Peptide-functionalized carbon nanotube (CNT) chemiresistor tests to evaluate the effect of the peptide conformations to VOC sensing: a) schematic views (top view (top) and side view (bottom)) of the chemiresistor platform; b) the scanning electron microscope image showing the peptide-functionalized CNT network between two gold electrodes; c) the representative response profile of the EP1-functionalized CNT chemiresistor in response to the isopropyl alcohol (IPA); d) the normalized resistance changes from the CNT chemiresistors depending on the functionalized peptides of EP1-5; e) the peptide conformation schematics showing how IPA molecules get access to the residues (blue-filled residue) with a high affinity to IPA.

uncharged  $\text{NH}_2$  groups.<sup>[60]</sup> The sharp  $\pi^*$  resonance  $\approx 401.3$  eV associated with the peptide bonds is the most appropriate feature to estimate the peptide's orientation on a substrate. To showcase the angle dependence in the N K-edge more immediately evident, the differential spectra between the normal ( $90^\circ$ ) and grazing ( $20^\circ$ ) radiation incidence are shown in Figure 3f. The peptide sequences EP1, EP2, and EP4 showed negative dichroism, indicating that the maximum radiation absorption occurred through the  $\pi^*$  orbitals positioned perpendicularly to the graphene surface, meaning that most peptide bonds were positioned in parallel<sup>[61]</sup> (top schematics in Figure 3g). EP3 and EP5 presented positive dichroism about the N1s  $\rightarrow \pi^*$  transition of the peptide (CONH) bond (bottom schematics in Figure 3g), indicating the maximum radiation absorption occurred when the amide  $\pi^*$  component orbitals oriented more parallel to the surface. In that case, most of the peptide bonds tend to be vertically oriented to the graphene surface. While corroborating the conformation of the most of the peptides predicted by MD simulations, EP4 exhibits discrepancies in alignment observed in NEXAFS experimentation, possibly due to peptide interaction differences between CNTs and graphene for this specific sequence. Figure S1a (Supporting Information) shows the intensity histogram of the solution color analyzed by the image process. EP4 has the lowest color intensity (darkest) (Figure S1b, Supporting Information), indicating significant

EP4 binding to carbon substrates (to both CNT and graphene). Due to the high surface area of CNT, EP4 would maintain its conformational shape (the top image of Figure S1c, Supporting Information). However, EP4 could be aggregated on the graphene surface (the bottom image of Figure S1c, Supporting Information), resulting in a low degree of freedom of NEXAFS spectra. We anticipate that consistent results could be obtained by reducing the EP4 concentration on the graphene. As a result, four peptides out of five exhibited good alignments between CNT-peptide interaction energies and NEXAFS spectra, supporting the feasibility of the peptide conformation prediction. In addition, more consistent alignments between interaction energy and NEXAFS could be obtained by utilizing identical substrates or optimizing the peptide functionalization.

To study how the peptide conformation affects VOC sensing in peptide-functionalized CNT sensors, we fabricated a chemiresistor platform (Figure 4a) consisting of a Si semiconductor substrate and silicon oxide ( $\text{SiO}_2$ ) dielectric layer, two Au electrodes with a  $5 \mu\text{m}$  gap. CNTs were assembled across the two electrodes, where the peptide functionalizes the CNTs. To assemble peptide-CNTs on the chemiresistor, we made a peptide-functionalized CNT solution by sonicating a peptide, a CNT, and ultra-purified water with a mixing ratio of 1 (mg):1 (mg):1 (mL), followed by the centrifuge to obtain evenly dispersed CNT solution. Then, the dielectrophoresis

(DEP) method assembled the peptide-CNT onto the 5  $\mu\text{m}$  gap. Figure 4b shows the scanning electron microscope (SEM) images showing the peptide-functionalized CNT network assembled across the two electrodes. When the IPA (25 ppm) is exposed to the peptide-CNT interface, the resistance of the CNT network changes, resulting in the measurable voltage changes in constant current bias. Figure 4c shows the representative IPA-response profile from the CNT chemiresistor functionalized by EP1. The normalized resistance change ( $\Delta R/R_0$ ) was defined as maximum resistance change ( $\Delta R$ ) divided by initial resistance ( $R_0$ ). We plotted the  $\Delta R/R_0$  as a chemiresistor response to IPA, depending on the functionalized peptides (Figure 4d), and compared the responses with the peptide conformations. Figure 4e shows the schematics of the peptide conformations showing how IPA molecules access the peptide-CNT interface. These schematics indicate that the differences in conformations provide different accessible surface areas for IPA, resulting in different  $\Delta R/R_0$ . IPA interaction energies were calculated (Table S2, Supporting Information) to identify the residues with a high affinity to IPA. The blue-filled circles indicate the IPA-affinity residue (i.e., the residues with a high affinity to IPA). A detailed description of the methodology for identifying IPA-affinity residues is in the Experimental Section. EP1 and EP2 are horizontal orientation to the CNT surface and have a larger surface area for IPA to access IPA-affinity residues. On the other hand, EP3, EP4, and EP5 are vertical orientation to the CNT surface and have a smaller surface area for IPA to access IPA-affinity residues. Therefore, EP1 and EP2 with larger accessible surface areas show higher responses in  $\Delta R/R_0$  than EP3-EP5.

To demonstrate whether the peptide conformation-induced surface area of the peptide-CNT interface affects other VOC sensing, we exposed acetone to the peptide-functionalized CNT chemiresistors, as shown in Figure S2 (Supporting Information). Interaction energies were calculated (Table S3, Supporting Information) to identify the acetone-affinity residues (yellow-filled circles, see Experimental Section for details). As EP1-EP5 are designed to be responsive to IPA, the  $\Delta R/R_0$  of acetone was lower than IPA (the bar graph in Figure S1, Supporting Information). However, EP1 and EP2 showed the highest responses while EP3 had the lowest, exhibiting a consistent tendency with IPA responses and supporting the peptide conformation as a significant role in VOC sensing.

To further demonstrate the effect of the peptide conformation, we tested chemiresistors functionalized by different peptides: 12-mer CNT-binding peptides (GSVQKLSATPWV (P1), ALNWTELHGQAT (P5), and LADNAFAHRQRC (P8)) identified by the normalized high-throughput sequencing phage display.<sup>[62]</sup> These peptides functionalized the CNTs, and we exposed IPA to these peptide-functionalized CNT chemiresistors. Figure S3a (Supporting Information) shows the  $\Delta R/R_0$  of the peptide-functionalized CNT chemiresistors in response to IPA. We calculated and obtained CNT interaction energies to P1, P5, and P8, as shown in Table S4 (Supporting Information), to predict the conformations of the P1, P5, and P8 (Figure S3b, Supporting Information). Interaction energies were calculated (Table S5, Supporting Information) to identify the IPA-affinity residues (blue-filled circles). The conformation of P5 is the less vertical orientation to CNT with the highest IPA response

result. On the other hand, P1 and P8 showed a more vertical orientation shape, resulting in lower IPA responses than P5. Importantly, this finding showcases that peptide conformation is critical in determining sensitivity under the CNT chemiresistor setting.

To investigate whether a hybrid peptide consisting of a CNT-binding sequence and a sequence identified for a target analyte can provide high sensitivity to VOCs, we tested chemiresistors functionalized by four hybrid peptides (P5-V11, P5-V12, P5-V21, and P5-V22), as shown in Figure S4a (Supporting Information). P5 served as the CNT-binding sequence combined with the previously reported short peptide sequences: IPA-responsive sequence (KSDSM) or acetone-responsive sequence (WHVSM).<sup>[34]</sup> One glycine served as a linker connecting P5 and KSDSM or WHVSM at N or C-terminus. This way, we anticipated that the peptide-CNT interface might operate appropriately in both binding to CNT and capturing the target VOC. However, we did not estimate the conformations of these peptides due to the long calculation time for interaction energies of the 18-mer sequences. As a result, the CNT chemiresistors functionalized by these peptides showed negligible responses to IPA and acetone (less than 2% resistance changes) (Figure S4b, Supporting Information), implying that the hybrid peptides do not work appropriately in the CNT chemiresistor platform. We suspect the hybrid peptides are 18-mer sequences with relatively long chains for functionalizing CNT, thus having more complex conformations that complicate sensing events. This result implies that when a specific peptide with a high affinity to target analytes functionalizes the CNT, how the CNT networks bind to the peptide can confound the peptide's functionality. Therefore, predicting how peptides interface with the CNT surface is imperative for evaluating peptide functionality for VOC sensing in the CNT sensors.

Overall, this study presented a multimodal method to identify and characterize peptide-based biorecognition on the CNT surface for building CNT-based VOC sensors. After a novel artificial neural networks algorithm identified five IPA-responsive peptide sequences, MD and NEXAFS N K-edge measurements characterized 2-dimensional modeling to predict the conformations of the peptides. We experimentally verified via in operando chemiresistor evaluation that this combination of characterizations effectively builds peptide-CNT pairs sensitive to gas-phase targets. This paper assumes that the peptide sequence has a single residue that links CNT and the residue with the highest interaction energy serves as the CNT linker. Then, the rest of the residues form an amino acid chain with a specific angle depending on the interaction energy (Table S1, Supporting Information) to predict the conformation of the peptide based on the interaction energy. Using this assumption, we consistently predicted the peptide conformation of EP1-5 (where EP1 and 2 were horizontally oriented and EP3-5 were vertically oriented), and the prediction was well aligned with the experiments (NEXAFS and chemiresistor). While we could account for multiple CNT linkers at a time, that leads to many possible conformations making prediction complicated. Therefore, we set consistent guidance to simplify the conformation model. In an actual situation, peptides are likely to have many different conformations on the CNT surface. In addition, the peptides are under dynamic conditions where their conformations

keep changing in real-time. Peptide–CNT interaction energies were obtained from the average of 10 independent simulation cycles. The higher standard deviation implies more dynamic and variable changes in peptide conformation in real situations. Therefore, the predicted peptide conformation shows the representative case that the peptide would form with a high probability. We theoretically anticipated that  $\approx 10\,000$  peptides would be on a CNT network of each device. The majority of peptides are likely to have the predicted conformation that significantly affects the electrical signal from the holistic system of the CNT–peptide interface. Therefore, the predicted peptide conformation is related to the probability, and a statistically meaningful number of peptides would lead this model to a good agreement with the chemiresistor data. The objective of the chemiresistor test in this manuscript is in operando evaluation of the peptide–CNT interface to observe VOC affinity in the form of electrical signature. The chemiresistor response depending on the different concentrations of the VOCs to evaluate gas sensing performance (e.g., linearity and the limit of detection) will be performed as a follow-up work to develop a gas sensor platform.

### 3. Conclusion

We demonstrate that the multimodal characterization using machine learning, MD, NEXAFS, and chemiresistor platform exhibited a novel way to analyze gas-phase peptide-based recognition elements and investigate how peptides–CNT interface functions toward VOC sensing. The results showed that the vertically oriented peptides on the CNT surface hinder VOC access to the peptide–CNT interface due to the low accessible surface area, resulting in a significantly lower sensor signal than the CNT chemiresistor with the horizontally oriented peptide. Our results strongly indicate that conformational characteristics of the peptide are critical in peptide–CNT devices for sensitive VOC sensing. This study is crucial for designing peptide-based biorecognition elements specific to target molecules and developing sensitive CNT-based chemical sensors.

### 4. Experimental Section

**Machine Learning and Molecular Dynamics for 7-mer Peptide Generations:** Machine learning was performed at the NNAlign server (<http://www.cbs.dtu.dk/services/NNAlign/>). The server generates artificial neural network models of peptide–VOC binding prediction. The input to the server is 5000 7-mer peptide sequences and their interaction energies to IPA. Feed-forward artificial network model with ten hidden neurons was used. The peptide is encoded to the network using the Blosum encoding method. It returns a sequence alignment, a binding motif of the interaction, and a model that can be used to scan for motif occurrences in new sequences. The gradient descent back-propagation algorithm lowered the sum of the squared errors between the predicted and given binding scores. A fivefold cross-validation technique evaluated the neural network by randomly splitting the data into five equally sized blocks (1000 peptides per block).

The MD simulation obtained IPA interaction energy that is input to the server. The more specific method to obtain peptide–IPA interaction energy is shown as follows: VMD1.9.3 made linear peptide models where the N-terminus and C-terminus are capped with patch ACE

and CT3, respectively. Then, NAMD2.13 carried out MD simulations with a temperature of 298.15 K, and the simulation length 10 ns. IPA molecule was placed 2.0 nm away from the center of mass of the peptide. Each system was minimized and equilibrated for 20 ns. For all production runs, snapshots collected every 500 ps for the last 5 ns of the simulation were used to calculate the interaction energy between a peptide and IPA.

**CNT and IPA/Acetone Interaction Energies to Peptides:** The pair-interaction energy between CNT and peptide was calculated using MD simulations to rank the binding affinity. The Single-wall carbon nanotube (SWCNT) model was constructed using Materials Studio 8.0 (©2014 Dassault Systèmes). Linear peptide models were made using VMD1.9.3<sup>[45]</sup> The N-terminus and C-terminus were capped with patch ACE and CT3, respectively. The CHARMM36 force field<sup>[63]</sup> was used to describe the interactions, while atom type CPT was used to characterize SWCNT. All MD simulations were carried out using the NAMD2.13 software package.<sup>[64]</sup> A nonbonded cutoff distance of 1.8 nm was used with the application of the switching function starting at 1.6 nm. The distance of the pair list was set at 2 nm. The temperature was set at 298.15 K. After 100 ns equilibration of peptide–SWCNT in water, water molecules were removed from each simulation system to mimic experimental conditions. It was assumed that the residues with the VOC interaction energies (in Tables S2, S3, and S5, Supporting Information) lower than  $-1\text{ kcal mol}^{-1}$  could serve as active residues with a high affinity to target VOC, indicated with a blue circle (for IPA affinity) or a yellow circle (for acetone affinity).

**Near-Edge X-Ray Absorption Fine Structure Spectroscopy (NEXAFS):** NEXAFS spectroscopy measurements were conducted at the SXR beamline of the Australian Synchrotron to probe N K-edge in partial electron yield (PEY) mode. All peptides were adsorbed on a multilayer CVD graphene film Si/SiO<sub>2</sub>/Ni wafer using a 1 mg mL<sup>-1</sup> peptide solution. A droplet of the solution was placed on each substrate for  $\approx 90\text{ s}$ , followed by removing the droplet to ensure minimal aggregation. The analysis of NEXAFS data was performed using the program QANT.<sup>[65]</sup>

**Materials:** Isopropyl alcohol (IPA) (C<sub>3</sub>H<sub>8</sub>O, 99.5%), acetone (C<sub>3</sub>H<sub>6</sub>O,  $\geq 99.5\%$ ) were purchased from Sigma-Aldrich (St. Louis, MO, USA). Carbon nanotube powder (small diameter SWNTs, HiPcoTM) was purchased from NanoIntegrals, Inc. (Skokie, IL, USA). All peptide sequences (with a purity of 90%) were purchased from Peptide 2.0 Inc. (Chantilly, VA, USA). Distilled water (UltraPure DNase/RNase-Free Distilled Water) was purchased from Life Technologies (Carlsbad, CA, USA). Multilayer CVD graphene film Si/SiO<sub>2</sub>/Ni wafer was purchased from Graphene Supermarket (Ronkonkoma, NY, USA).

**Device Fabrication:** The fabrication process for the chemiresistor platform started with a 4-in. silicon wafer (0.5 mm—thickness) with a 0.2  $\mu\text{m}$ —thickness SiO<sub>2</sub> top layer. After the wafer cleaning process by sequential spraying of acetone, IPA, deionized (DI) water, and IPA, photoresists of LOR10A and AZ514 were spin-coated for photolithography pattern windows for the source and drain electrodes. Next, a thermal evaporator deposited 15 nm/65 nm thickness of Ti/Au layer onto the photoresist pattern with a 0.1 nm s<sup>-1</sup> rate. Then, a lift-off process was applied by taping-stripping, spraying acetone, dipping in a developing solution (1165), and plasma-etching. Finally, the individual FET chipset is completed by dicing the wafer using a dicing saw. The total dimensions of the platform were 18 mm—width  $\times$  8.5 mm—length  $\times$  0.5 mm—thickness.

**Peptide-Functionalized CNT Solution:** The assembly of the peptide-functionalized CNTs onto the chemiresistor platform had two steps of 1) the peptide–CNT solution preparation and 2) the dielectrophoresis (DEP) process. A peptide-functionalized CNT solution preparation started by putting 150  $\mu\text{L}$  of a peptide solution (1.5 mg peptide + 150  $\mu\text{L}$  ultra-purified water), 1.5 mg of a CNT powder, and 1.35 mL of ultra-purified water into a falcon tube. A sonicating probe connected to an ultrasonic generator (5300, Ultrasonic Power Corporation, Freeport, IL, USA) was used to facilitate the mix of the solution, with the following conditions:  $-37$  power level, 0.5 repeating duty cycle, and 30 min duration. The solution was then centrifuged to separate the residual

CNTs, forming a (mostly) evenly dispersed CNT solution. For the CNT solution without peptide, all solution preparation process was the same except for using SDS instead of the peptide. The DEP process was performed for the assembly of the peptide-functionalized CNTs onto the chemiresistor platform. First, 10  $\mu\text{L}$  of the solution was pipetted across the electrode gaps, and then an AC voltage of 6  $V_{p-p}$ , 10 MHz, and 10 s was applied. The DEP force aligns the peptide-CNTs across the electrode gap. After rinsing with deionized water and blow drying with house air, the peptide-functionalized CNT chemiresistor was completed. The CNT bundles formed across the gap between two electrodes were checked by measuring an electrical resistance level. Assembled CNTs were also observed by an optical microscope (Axio Imager.M2m, Carl Zeiss Microscopy GmbH, Jena, Germany) and a scanning electron microscope (SEM) (SU70, Hitachi, Tokyo, Japan).

**Gas Exposure Setup and Protocols:** An acrylic chamber was used as an experimental setup for the VOC exposure test. The configuration of the acrylic chamber is composed of an air inlet/outlet for the purging/ventilation, a VOC injection port, a temperature/humidity sensor, a small fan for facilitating the air circulation, and the CNT chemiresistor clipped by an electrical connection jig (or clamshell). The clamshell is electrically connected to the semiconductor analyzer (Keithley 4200A-SCS, Tektronix, Beaverton, OR, USA) that generates a constant current, measures a voltage, and records measurement data. The semiconductor analyzer includes a switching matrix (Keithley 708B, Tektronix, Beaverton, OR, USA) that enables multiplexing up to 12 pairs of electrodes serially and continuously. The semiconductor analyzer measured voltage responses from the CNT FET when the applied constant current was 1  $\mu\text{A}$ , and the sampling rate was about 3 s. The total measurement time was 1500 s, where 25 ppm of VOC was injected at 500 s, and evacuated by purging at 1000 s. The voltage output of the responses was converted to the resistance values by dividing the measured voltage responses by the constant current of 1  $\mu\text{A}$ . Baseline drift was corrected by subtracting a linear fitting line (obtained from the least-square regression method) drawn from the initial profile from 0 to 500 s of the experiment. The magnitude response ( $\Delta R$ ) was defined as the maximum change in resistance at 1000 s.

## Supporting Information

Supporting Information is available from the Wiley Online Library or from the author.

## Acknowledgements

All authors acknowledge funding support from the U.S. Air Force Research Laboratory. All authors acknowledge cleanroom facility support from the Sensors Directorate in the U.S. Air Force Research Laboratory. This research was performed while D.S. held an NRC Research Associateship award at the U.S. Air Force Research Laboratory. N.B. acknowledges funding support from the Air Force Office of Scientific Research (FA9550-20-1-0430). NEXAFS measurements were performed at the SXR beamline of the Australian Synchrotron, an ANSTO facility. All authors would like to thank Lars Thomsen for assistance with NEXAFS measurements.

## Conflict of Interest

The authors declare no conflict of interest.

## Data Availability Statement

The data that support the findings of this study are available from the corresponding author upon reasonable request.

## Keywords

peptide biorecognition elements, peptide conformation prediction, volatile organic compounds, human performance-indicative biomarkers, carbon nanotube chemiresistors

Received: August 2, 2022

Revised: September 30, 2022

Published online:

- [1] D. M. Ruszkiewicz, D. Sanders, R. O'Brien, F. Hempel, M. J. Reed, A. C. Riepe, K. Bailie, E. Brodrick, K. Darnley, R. Ellerkmann, O. Mueller, A. Skarysz, M. Truss, T. Wortelmann, S. Yordanov, C. L. P. Thomas, B. Schaaf, M. Eddleston, *EclinicalMedicine* **2020**, 29–30, 100609.
- [2] M. Khoubnasabjafari, V. Jouyban-Gharamaleki, R. Ghanbari, A. Jouyban, *Bioanalysis* **2020**, 12, 1195.
- [3] Y. H. Ngo, M. Brothers, J. A. Martin, C. C. Grigsby, K. Fullerton, R. R. Naik, S. S. Kim, *ACS Omega* **2018**, 3, 6230.
- [4] F. Pabst, W. Miekisch, P. Fuchs, S. Kischkel, J. K. Schubert, *J. Cardio-thorac. Surg.* **2007**, 8, 37.
- [5] S. W. Harshman, B. A. Geier, A. V. Qualley, L. A. Drummond, L. E. Flory, M. Fan, R. L. Pitsch, C. C. Grigsby, J. B. Phillips, J. A. Martin, *J. Breath Res.* **2017**, 11, 047111.
- [6] M. Maniscalco, G. De Laurentiis, C. Pentella, M. Mormile, A. Sanduzzi, M. Sofia, G. De Laurentiis, C. Pentella, M. Mormile, A. Sanduzzi, *Biomarkers* **2006**, 11, 233.
- [7] D. Sim, M. C. Brothers, J. M. Slocik, A. E. Islam, B. Maruyama, C. C. Grigsby, R. R. Naik, S. S. Kim, *Adv. Sci.* **2022**, 9, 2104426.
- [8] A. Tricoli, N. Nasiri, S. De, *Adv. Sci. News* **2017**, 27, 1605271.
- [9] N. Kyoung, T. Sun, D. La, J. Hoon, Y. Woo, Y. Shin, *Sens. Actuators, B* **2010**, 147, 55.
- [10] C. H. Park, V. Schroeder, B. J. Kim, T. M. Swager, *ACS Sens.* **2018**, 3, 2432.
- [11] S. Ju, K.-Y. Lee, S.-J. Min, Y. K. Yoo, K. S. Hwang, S. K. Kim, *Sci. Rep.* **2015**, 59196, 9196.
- [12] A. H. J. Kolk, J. J. B. N. Van Berkel, M. M. Claassens, E. Walters, S. Kuijper, J. W. Dallinga, F. J. Van Schooten, *Int. J. Tuberc. Lung Dis.* **2012**, 16, 777.
- [13] N. Fens, M. P. van der Schee, P. Brinkman, P. J. Sterk, *Clin. Exp. Allergy* **2013**, 43, 705.
- [14] S. W. Harshman, B. A. Geier, M. Fan, S. Rinehardt, B. S. Watts, L. A. Drummond, G. Preti, J. B. Phillips, D. K. Ott, C. C. Grigsby, *J. Breath Res.* **2015**, 9, 47103.
- [15] S. Pyo, K. Lee, T. Noh, E. Jo, J. Kim, *Sens. Actuators, B* **2019**, 288, 618.
- [16] F. M. Peng, P. H. Xie, Y. G. Shi, J. D. Wang, W. Q. Liu, H. Y. Li, *Chromatographia* **2007**, 65, 331.
- [17] M. Akbar, H. Shakeel, M. Agah, *Lab Chip* **2015**, 15, 1748.
- [18] V. Schroeder, S. Savagatrup, M. He, S. Lin, T. M. Swager, *Chem. Rev.* **2018**, 119, 599.
- [19] A. E. Islam, J. A. Rogers, M. A. Alam, *Adv. Mater.* **2015**, 27, 7908.
- [20] B. L. Allen, P. D. Kichambare, A. Star, *Adv. Mater.* **2007**, 19, 1439.
- [21] T. H. Kim, B. Y. Lee, J. Jaworski, K. Yokoyama, W. Chung, E. Wang, S. Hong, A. Majumdar, S. Lee, K. I. M. E. T. Al, *ACS Nano* **2011**, 5, 2824.
- [22] X. Xu, P. Clément, J. E.-O. Sterberg, N. Kelley-Loughnane, K. Møth-Poulsen, J. L. Chávez, M. Palma, *Nano Lett.* **2018**, 18, 4130.
- [23] D. Sim, R. Krabacher, J. L. Chavez, J. A. Martin, A. E. Islam, Z. Kuang, B. Maruyama, R. R. Naik, S. S. Kim, *2019 IEEE Int. Flex. Electron. Technol. Conf. (IFETC)*, IEEE, Vancouver, BC, Canada **2019**.

- [24] Z. Kuang, S. N. Kim, W. J. Crookes-goodson, B. L. Farmer, *ACS Nano* **2010**, *4*, 452.
- [25] N. T. Tung, P. T. Tue, T. Thi, N. Lien, Y. Ohno, *Sci Rep.* **2017**, *7*, 17881.
- [26] Z. Kuang, S. S. Kim, Y. H. Ngo, M. C. Mcalpine, B. L. Farmer, R. R. Naik, Z. Kuang, M. C. Mcalpine, B. L. Farmer, *Biointerphases* **2016**, *11*, 041003.
- [27] J. A. Martin, Y. Chushak, J. L. Chávez, J. A. Hagen, N. Kelley-loughnane, *J. Nucleic Acids* **2016**, *2016*, 9718612.
- [28] J. Hagen, W. Lyon, Y. Chushak, M. Tomczak, R. Naik, M. Stone, N. Kelley-Loughnane, *ACS Chem. Neurosci.* **2013**, *4*, 444.
- [29] X. Xiao, Z. Kuang, J. M. Slocik, S. Tadepalli, M. Brothers, S. Kim, P. A. Mirau, C. Butkus, B. L. Farmer, S. Singamaneni, C. K. Hall, R. R. Naik, *ACS Sens.* **2018**, *3*, 1024.
- [30] N. Nakatsuka, K. A. Yang, J. M. Abendroth, K. M. Cheung, X. Xu, H. Yang, C. Zhao, B. Zhu, Y. S. Rim, Y. Yang, P. S. Weiss, M. N. Stojanović, A. M. Andrews, *Science* **2018**, *362*, 319.
- [31] S. Kim, L. Xing, A. E. Islam, M. Hsiao, Y. Ngo, O. M. Pavlyuk, R. L. Martineau, C. M. Hampton, C. Crasto, J. Slocik, M. P. Kadakia, J. A. Hagen, N. Kelley-loughnane, R. R. Naik, L. F. Drummy, *ACS Appl. Mater. Interfaces* **2019**, *11*, 13927.
- [32] Z. Zhang, W. Zhu, T. Kodadek, *Nat. Biotechnol.* **2000**, *18*, 71.
- [33] C. Yue, N. K. Sang, R. N. Rajesh, *Acc. Chem. Res.* **2012**, *45*, 696.
- [34] M. Mascini, D. Pizzoni, G. Perez, E. Chiarappa, C. Di, P. Pittia, D. Compagnone, *Biosens. Bioelectron.* **2017**, *93*, 161.
- [35] M. Mascini, S. Gaggiotti, F. Della Pelle, C. Di Natale, S. Qakala, E. Iwuoha, P. Pittia, D. Compagnone, *Front. Chem.* **2018**, *6*, 105.
- [36] S. Ju, K. Y. Lee, S. J. Min, Y. K. Yoo, K. S. Hwang, S. K. Kim, H. Yi, *Sci. Rep.* **2015**, *5*, 9196.
- [37] J. S. Weerakkody, M. El Kazy, E. Jacquier, P. H. Elchinger, R. Mathey, W. L. Ling, C. Herrier, T. Livache, A. Buhot, Y. Hou, *ACS Nano* **2022**, *16*, 4444.
- [38] S. Gaggiotti, F. Della Pelle, M. Mascini, A. Cichelli, *Sensors* **2020**, *20*, 4433.
- [39] M. Tanaka, T. Minamide, Y. Takahashi, Y. Hanai, T. Yanagida, M. Okochi, *Chem. Lett.* **2019**, *48*, 978.
- [40] A. J. M. Barbosa, A. R. Oliveira, A. C. A. Roque, *Trends Biotechnol.* **2018**, *36*, 1244.
- [41] S. Gaggiotti, C. Hurot, J. S. Weerakkody, R. Mathey, A. Buhot, M. Mascini, Y. Hou, D. Compagnone, *Sens. Actuators, B* **2020**, *303*, 127188.
- [42] S. Hong, T. H. Park, *Anal. Chem.* **2016**, *88*, 11283.
- [43] B. Alvarez, B. Reynisson, C. Barra, S. Buus, N. Ternette, T. Connelley, M. Andreatta, Nielsen, *Mol. Cell. Proteomics* **2019**, *18*, 2459.
- [44] M. Nielsen, M. Andreatta, *Nucleic Acids Res.* **2017**, *45*, W344.
- [45] W. Humphrey, A. Dalke, K. Schulten, *J. Mol. Graphics* **1996**, *14*, 33.
- [46] X. Liu, F. Zheng, A. Jürgensen, V. Perez-Dieste, D. Y. Petrovykh, N. L. Abbott, F. J. Himpfel, *Can. J. Chem.* **2007**, *85*, 793.
- [47] B. O. Leung, J. L. Brash, A. P. Hitchcock, *Materials* **2010**, *3*, 3911.
- [48] P. Wu, Y. Yu, C. E. McGhee, L. H. Tan, Y. Lu, *Adv. Mater.* **2014**, *26*, 7849.
- [49] M. M. Nahid, E. Gann, L. Thomsen, C. R. McNeill, *Eur. Polym. J.* **2016**, *81*, 532.
- [50] S. Franchi, C. Battocchio, M. Galluzzi, E. Navisse, A. Zamuner, M. Dettin, G. Iucci, *Mater. Sci. Eng. C* **2016**, *69*, 200.
- [51] V. Secchi, S. Franchi, M. Santi, A. Vladescu, M. Braic, T. Skála, J. Nováková, M. Dettin, A. Zamuner, G. Iucci, C. Battocchio, *Nanomaterials* **2018**, *8*, 148.
- [52] T. Weidner, D. G. Castner, *Phys. Chem. Chem. Phys.* **2013**, *15*, 12516.
- [53] Z. E. Hughes, T. R. Walsh, *J. Mater. Chem. B* **2015**, *3*, 3211.
- [54] N. Dragneva, W. B. Floriano, D. Stauffer, R. C. Mawhinney, G. Fanchini, O. Rubel, *J. Chem. Phys.* **2013**, *139*, 174711.
- [55] R. B. Pandey, Z. Kuang, B. L. Farmer, S. S. Kim, R. R. Naik, *Soft Matter* **2012**, *8*, 9101.
- [56] Z. E. Hughes, S. M. Tomásio, T. R. Walsh, *Nanoscale* **2014**, *6*, 5438.
- [57] C. Rajesh, C. Majumder, H. Mizuseki, Y. Kawazoe, *J. Chem. Phys.* **2009**, *130*, 124911.
- [58] G. Raffaini, F. Ganazzoli, *Langmuir* **2013**, *29*, 4883.
- [59] Z. Gu, Z. Yang, Y. Chong, C. Ge, J. K. Weber, D. R. Bell, R. Zhou, *Sci. Rep.* **2015**, *5*, 10886.
- [60] M. B. Ebrahim-Habibi, M. Ghobeh, F. A. Mahyari, H. Rafii-Tabar, P. Sasanpour, *Sci. Rep.* **2019**, *9*, 1273.
- [61] Y. Zubavichus, A. Shaporenko, M. Grunze, M. Zharnikov, *J. Phys. Chem. B* **2007**, *111*, 9803.
- [62] R. Krabacher, S. Kim, Y. Ngo, J. Slocik, C. Harsch, R. Naik, *Chem- osensors* **2021**, *9*, 201.
- [63] J. Huang, A. D. Mackerell, *J. Comput. Chem.* **2013**, *34*, 2135.
- [64] J. C. Phillips, R. Braun, W. Wang, J. Gumbart, E. Tajkhorshid, E. Villa, C. Chipot, R. D. Skeel, L. Kalé, K. Schulten, *J. Comput. Chem.* **2005**, *26*, 1781.
- [65] E. Gann, C. R. McNeill, A. Tadich, B. C. C. Cowie, L. Thomsen, *J. Synchrotron. Radiat.* **2016**, *23*, 374.